Soft Computing (2022) 26:6021–6040
https://doi.org/10.1007/s00500-022-07049-0

FUZZY SYSTEMS AND THEIR MATHEMATICS

A New single switch DC-DC converter for PEM fuel cell-based electric vehicle system with an improved beta-fuzzy logic MPPT controller

C. H. Hussaian Basha[1] · C. Rani[2]

Accepted: 19 March 2022 / Published online: 16 May 2022

Abstract

The fuel cell-based electric power generation system is playing a major role in the present electrical power distribution system. The fuel cell gives a nonlinear V-I curve. As a result, the extraction of fuel cell power is very difficult. To extract the peak power of the fuel cell, a Maximum Power Point Tracking (MPPT) technique is used. In this work, an Improved Beta-based Fuzzy Logic Controller (IBeta-FLC) is proposed to track the MPP with high speed. The proposed MPPT technique is compared with other hybrid MPPT techniques in terms of maximum power extraction, settling time, oscillations across MPP, tracking speed, and efficiency. The Proton Exchange Membrane Fuel Cell (PEMFC) stack gives high output current, and low output voltage. As a result, the overall system conduction losses are improved. So, in this work, a new Single Switch Universal Input-voltage Boost Converter (SSUIBC) is introduced to step-up the fuel cell output voltage. The features of the proposed boost converter are high voltage gain, less complexity in design, wide output operation, and less voltage stress across the switch. The proposed PEMFC fed boost converter system performance is evaluated successfully by using a MATLAB/Simulink window. In addition, the utilized boost converter is investigated experimentally by using an external DC-source.

Keywords Duty cycle · Hybrid fuzzy logic controllers · High voltage conversion ratio · MPPT · PEMFC stack · And soft output characteristics of the fuel stack

Abbreviations

SSUIBC	Single Switch Universal Input-voltage Boost Converter
IR	Incremental Resistance
V_{FC}	Voltage of PEMFC stack
I_{FC}	Current of PEMFC stack
IHC-FLC	Improved Hill Climb-based Fuzzy Logic Controller
VSS-P&O	Variable Step Size Perturb & Observe
ZVS	Zero Voltage Switching
IDD	Interleaved Dual Diode
CCM	Continuous Conduction Mode of Operation
DCM	Discontinuous Conduction Mode of Operation
V_{Ohmic}	Ohmic region voltage of PEMFC
V_{Active}	Active region voltage of PEMFC
V_{Concen}	Concentrated region voltage of PEMFC
T_{FCop}	PEMFC operating voltage
P_{H_2}	Hydrogen partial pressure
O_{H_2}	Oxygen partial pressure
RH_{Ano}	Humidity vapor at anode of PEMFC
RH_{Cat}	Humidity vapor at cathode of PEMFC
P_{Ano}	Inlet pressure of anode in PEMFC
P_{Cat}	Inlet pressure of cathode in PEMFC
$P_{H_2o}^{Sat}$	Saturation pressure of water vapor
$J = I_{cell}/A$	Variation of fuel cell current with respect to its area
R_{ef}	Specific resistivity of electrolyte
$X_1^{(1)} = V_{FC}$	Input layer first node input
$X_2^{(1)} = I_{FC}$	Input layer second node input
$net_P^{(1)}$	Input layer net input
$Y_P^{(1)}(k)$	Input layer output
$net_q^{(1)}$	Second layer net input

✉ C. H. Hussaian Basha
sbasha238@gmail.com

C. Rani
crani@vit.ac.in

[1] K.S.R.M. College of Engineering (Autonomous), Kadapa, AP, India

[2] School of Electrical Engineering, VIT University, Vellore, India

$Y_q^{(1)}(k)$	Second layer output
Σ_q	Gaussian membership function mean
μ_q	Standard mean value
$\text{net}_r^{(3)}$	Output layer output node net input
$Y_q^{(1)}(k)$	Output layer output node output
W	Weight connected between two neurons
S_P	Slope of the V-I curve
S_{T_new}	New step size value of FLC- VSSIC
S_{T_old}	Previous step size value of FLC- VSSIC
V_{Lx}, V_{Ly} and V_{Lz}	SSUIBC Inductor voltages
D(k-1), and *D(k)*	Variation of duty values
V_{Cx}, V_{Cy} and V_{Ca}	Capacitor voltages of SSUIBC
I_{Lx}, I_{Ly}, and I_{Lz}	Inductor currents of SSUIBC
V_{Dx}, V_{Dy}, V_{Dz}	Diode voltages of boost converter
Gain_{CCM}	Gain of SSUIBC under CCM
Gain_{DCM}	Gain of SSUIBC under DCM
error	Resultant signal of RBFN controller
V_D/V_0	Diode voltage stress of converter
V_Q/V_0	MOSFET voltage stress of converter

1 Introduction

From the continuous increment of fossil fuels cost and its less availability, most of the automotive industries are focusing on alternative energy sources which are ultra-capacitors, batteries, and fuel cells (Fu, et al. 2021). The features of fuel cell power generation systems are less noise, a long lifetime period, high energy density, less CO_2 emission, and high-efficiency when compared to the solar and wind power generation systems. In addition, it does not affect the environmental conditions and gives a continuous power supply to the electric vehicle during all spells as long as fuel is offered. From the literature survey (https://www.marketsandmarkets.com/Market-Reports/fuel-cell-market-348.html), it is clearly observed that the fuel cell demand is increasing every year. From the world fuel cell market survey, the fuel cell power generation cost may reach 848 million US dollars by 2025. Based on the kind of electrolyte substance recycled, the fuel cells are characterized as Photonic Ceramic Fuel Cell (PCFC), Direct Methanol Fuel Cell (DMFC), Zinc Air Fuel Cell (ZAFC), Phosphoric Acid-based Fuel Cell (PAFC), Proton Exchange Membrane Fuel Cell (PEMFC), Alkaline Fuel Cell (AFC), and Solid Oxide Fuel Cell (SOFC) (Zakaria, et al. 2021).

Among all of the fuel cells, the PEMFC is the most popular and predominately used for electric vehicle application and distributed energy systems in order to meet the required load demand. In addition, the merits of the PEMFC stack are low corrosion, small in size, easy to construct, less working temperature, fast start-up, and very high power density (Alaswad, et al. 2021). The PEMFC stack gives nonlinear voltage versus current characteristics, and it consists of a unique operating power point. The operating point varies based on the fragmentary pressure of hydrogen. In order to maintain the operating point constant at the peak power point, an MPPT method is applied in article (Mallick and Mukherjee 2020) for enhancing the performance of the fuel cell stack.

At present, most of the research scholars focusing on computational intelligence-based MPPT techniques for solving the nonlinear issues of PEMFC-based power generation system (Salvado, et al. 2021). The merits of these techniques are more flexible, easy to implement, and highly robust when compared to the other conventional MPPT techniques. In this work, an Improved Beta-Fuzzy Logic Controller (IBeta-FLC) is proposed and it is compared with other hybrid fuzzy logic-based MPPT controllers in terms of tracing speed, fuel cell output power, and settling time of converter output voltage. The compared power point tracking methods are Variable Step Size Perturb and Observe (VSS-P&O), Radial Basis Functional Network (RBFN), Fuzzy Logic Controller-based Variable Step Size Incremental Conductance (FLC-VSSIC), and Fuzzy Logic Controller-based Improved Hill Climb (FLC-IHC). The fuel cell output voltage (V_{FC}) and current (I_{FC}) are given to the proposed hybrid MPPT controller in order to find out the required duty cycle of the boost converter.

The PEMFC stack gives a high output current and less output voltage which is not desirable for industrial loads and electric vehicle applications. So, the fuel cell stack cannot be directly connected to the load. The high step-up circuit topology is placed in between the source and load in order to improve the fuel cell output power. For limiting the disadvantages of conventional boost converters, in this work, a single switch, universal input voltage, wide input and output operation-based boost converter is introduced (see in Fig. 1) to improve the power transfer efficiency of a fuel cell stack system.

2 Literature survey

From the literature survey (Naseri, et al. 2018), the most frequently used MPPT method is Perturb & Observe (P&O). In this technique, the trial and error process is

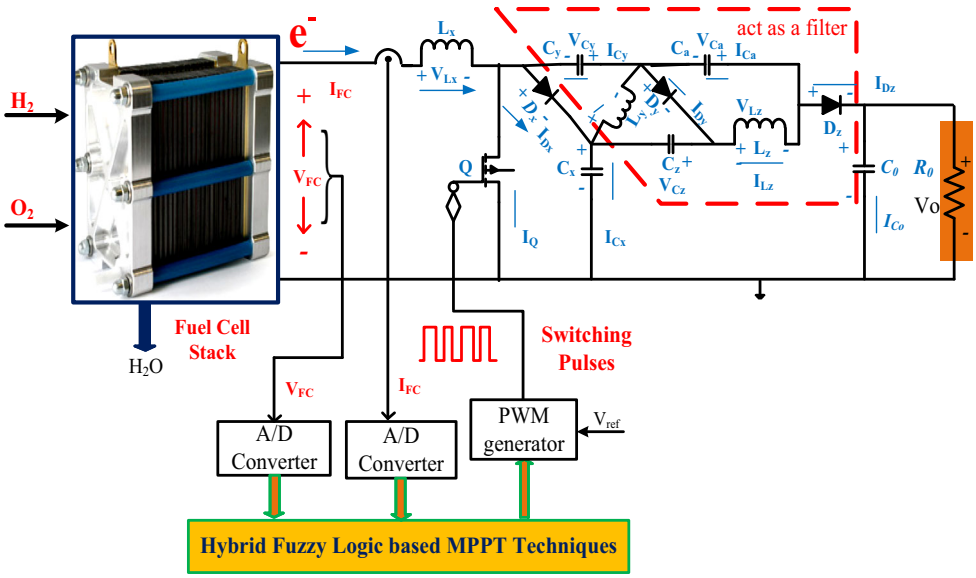

Fig. 1 Block diagram of PEMFC fed single switch transformerless UIBC system

recommended to extract the extreme power of the fuel cell stack. At each and every point on *V-I* characteristics, the sensors are used to determine the PEMFC stack voltage and current. After that, the calculated power is compared with the existed power. If the change of power consists of the + ve sign, then it perturbs in the same direction or, otherwise, the perturbation has been done in the opposite way. The demerits of P&O technique are compensated by applying an Incremental Conductance (IC) power point tracing method.

In IC technique, the PEMFC power is perturbed by using the instantaneous conductance of the fuel cell. Here, the slope of the *V-I* curve is considered to trace the MPP of fuel cell. At MPP, the slope of the *V-I* curve is zero and it is + ve when the working point of PEMFC is left side of the *V-I* curve. Otherwise, it is −ve when the working point is on the right side of the MPP (Harrag and Messalti 2017). The drawback of this method is high design complexity when compared to the P&O.

In article (Shetty and Chakrasali 2020), a Hill Climb (HC) method is applied to transfer the maximum power of the PEMFC stack from source to load. The working principle of this method is similar to the conventional P&O. Here, the fuel cell voltage (V_{FC}) is used as a reference variable for obtaining the required duty value of the dc–dc converter. The drawback of this method is excessive power loss at the time of step change of power. So, an Improved Beta-Fuzzy Logic Controller is proposed for the effective operation of fuel cell stack.

Another drawback of fuel cell is low output voltage. So, different kinds of dc-dc boost converters are used to improve the power transfer capability of PEMFC stack and which are organized as isolated boost converters and non-isolated boost converters. The major drawback of solid oxide-based fuel cell power generation system is high installation cost. A low cost isolated boost converter is used in article (Török, et al. 2019) to reduce the overall fuel cell power generation cost. The drawback of this converter is high design complexity. In article (Zhou, et al. 2019), a quasi-Z source, and isolated boost converter is used in a fuel cell distribution power generation system to increase the power density of the system.

However, the isolated boost converters are having the drawbacks of high implementation cost, and more complexity in design. In addition, it requires an additional high switching frequency transformer to eliminate the DC-link between the source and load. So, the drawbacks of the isolated converters are overcome by using the non-isolated boost converters. The merits of non-isolated boost converters are less cost, compact in size, and high efficiency (Garrigós et al. 2019).

In article (Villarreal-Hernandez, et al. 2020), an Interleaved Double Dual (IDD), non-isolated dc-dc converter, is used in fuel stack-based electric vehicle application. The merits of this converter are high voltage conversion ratio and less switching losses. Here, an interleaved concept is used to solve the issue of low output voltage plus high output current of PEMFC stack. The drawback of this converter is pulsating output current and high voltage stress on power switches. To overcome the drawbacks of IDD boost converter, a cascaded two-phase interleaved and two level boost converters are used in article (Ma, et al. 2019) to increase the voltage conversion ratio of a fuel stack. The drawback of this topology is required high number of power semiconductors.

In article (Thounthong, et al. 2021), a high step-up, switched inductor, multiphase, and an interleaved dc-dc converter is explained to obtain the continuous output

power of the fuel cell-based hybrid distribution power generation system. A multi-switch, an interleaved dc-dc converter is used in the PEMFC to enhance its dynamic response (Habib et al. 2017). In addition, the authors analyzed the performance of 5 kW fuel cell fed boost converter system at different operating temperature circumstances. From the software and hardware results, the authors says that the multi-switch converter voltage conversion ratio is improved when its corresponding duty cycle is increased.

In article (Youn, et al. 2020), the authors investigated the hybrid, interleaved boost converters at Discontinuous Conduction Mode (DCM) of operation for the application of fuel cell-based induction motor drive system. From the performance results, the authors says that the proposed converter is operating effectively and efficiently at DCM of operation. The drawback of this converter is high conduction losses. Here, a SSUIBC is proposed and it is implemented by interconnecting a circuit ($D^2C^3L^2$) in middle of the basic dc–dc converter and consumer load (R_0). The interfaced network acts as a filter and it is used to suppress the capacitor voltage distortions and inductor current ripples. In addition, it improves voltage profile of the converter and reduces the voltage stress across the power semiconductor devices. From Fig. 1, it is clearly observed that the input supply terminal of the converter is connected to the output negative terminal. As a result, the parasitic capacitance is bypassed to remove the undesirable leakage currents.

3 Modelling of PEM fuel cell

The PEM fuel cell is an electrochemical instrument which translates the chemical energy into electrical energy. The block diagram of PEM fuel cell plus its electrical equivalent circuits are shown in Fig. 2a and b (Kurnia, et al. 2021). It comprises the three main parts which are anode, cathode and electrolyte. The electrolyte is inserted in middle of the anode plus cathode. The electrolyte is designed by using a polymer electrolyte membrane. From Fig. 2a, it is clearly given that the hydrogen (H_2) and oxygen (O_2) are the inputs to the fuel cell stack. The hydrogen and oxygen are compressed and humidified with the help of air compressor and humidifier.

The pressurized hydrogen gas flows toward the anode is divided into protons and electrons. The electrons are transferred from anode to the outside circuit for generating the electricity. The protons flow from the anode to cathode via electrolyte membrane layer which reacts through the oxygen atoms to harvest the heat and water. From Fig. 2a, the anode and cathode side chemical reactions are derived as follows (Banham, et al. 2018):

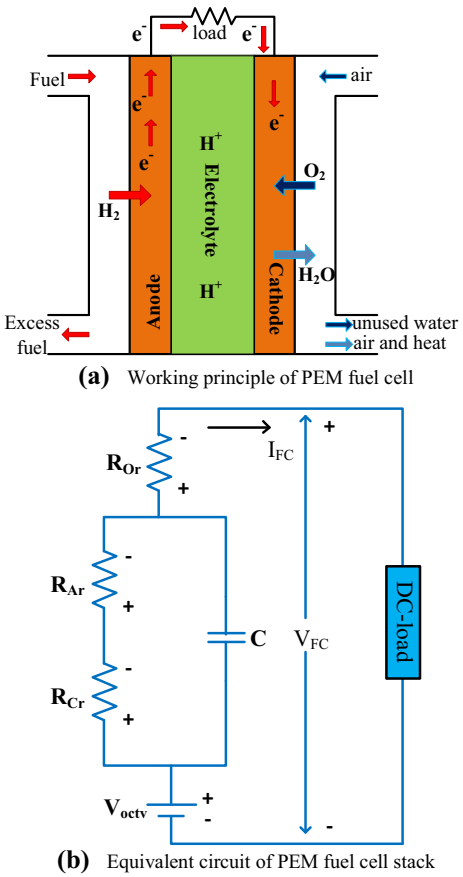

Fig. 2 **a** Working principle of PEM fuel cell. **b** Equivalent circuit of PEM fuel cell stack

$$H_2 \Rightarrow 2H^+ + 2e^- \tag{1}$$

$$2H^+ + 2e^- + \frac{1}{2}O_2 \Rightarrow H_2O \tag{2}$$

$$H_2 + \frac{1}{2}O_2 \Rightarrow H_2O + \text{energy} \tag{3}$$

The total voltage generation of the fuel cell stack is determined by using Eq. (4).

$$V_{\text{total}} = nV_{\text{FC}} \tag{4}$$

where 'n' indicates the total number fuel cells in the PEMFC stack and 'V_{FC}' is each cell output voltage which is derived as (Ijaodola et al. 2019),

$$V_{\text{FC}} = E_{\text{Octv}} - V_{\text{Ohmic}} - V_{\text{Active}} - V_{\text{Concen}} \tag{5}$$

where 'EOctv' is the open circuit thermodynamic voltage which is derived as follows:

$$E_{\text{Octv}} = 1.29 - 0.8e^{-3}\left(T_{\text{FCop}} - 298.12\right) + \lambda \tag{6}$$

$$\lambda = 4.3e^{-5} * \log(P_{H_2}\sqrt{P_{O_2}})T_{\text{FCop}} \tag{7}$$

where TFCop is the fuel cell operating temperature. The

partial pressure of hydrogen (P_{H_2}) and oxygen (P_{O_2}) is derived as follows:

$$P_{H_2} = \frac{1}{2} RH_{Ano} P^{sat}_{H_2O} \left(\frac{1}{\frac{RH_{Ano} * P^{sat}_{H_2O}}{P_{Ano}} * \exp\left(\frac{1.6*(I_{cell}/A)}{T_{FCop}}\right)} \right) \quad (8)$$

$$P_{O_2} = \frac{1}{2} RH_{Cat} P^{sat}_{H_2O} \left(\frac{1}{\frac{RH_{Cat} * P^{sat}_{H_2O}}{P_{Cat}} * \exp\left(\frac{4.1*(I_{cell}/A)}{1.33*T_{FCop}}\right)} \right) \quad (9)$$

where RH_{Ano}, and RH_{Cat} are the relative humidity vapors at anode and cathode. Similarly, P_{Ano} and P_{Cat} are the inlet pressures of anode and cathode, respectively. Finally, 'A,' 'I_{cell},' and $P^{sat}_{H_2O}$ are the electrode area, fuel cell current, and saturation pressure of water vapor, respectively. The active, ohmic, and concentration polarization losses are derived as follows:

$$V_{Active} = C_1 + C_2 T_{FCop} + (C_3 + C_4) T_{FCop} * \log(C_{O_2} + I_{cell}) \quad (10)$$

$$V_{Concen} = -\frac{RT_{FCop}}{nF} \log\left(1 - \frac{j}{j_{max}}\right) \quad (11)$$

$$V_{Ohmic} = I_{cell} * (R_{ef} + R_{pf}) \quad (12)$$

From Eq. (10), C_1, C_2, C_3, and C_4 are the empirical coefficients of each fuel cell. The concentrated oxygen (C_{O_2}) is derived as follows:

$$C_{O_2} = \frac{P_{O_2}}{5.08e^6 * \exp(-498/T_{FCop})} \quad (13)$$

Similarly, from Eqs. (12), and (13), the current density (j) and electron flow equivalent resistance (R_{ef}) are derived as follows:

$$j = \frac{I_{cell}}{A} \quad (14)$$

$$R_{ef} = \frac{\gamma_{ef} * Q}{A} \quad (15)$$

From Eq. (15), the membrane specific resistivity is derived as follows:

$$\gamma_{ef} = \frac{181.6\left[1 + 0.03j + 0.62(T_{FCop}/303)^2 j^{2.5}\right]}{(W - 0.634 - 3j) * \exp\left(\frac{4.18(T_{FCop}-303)}{T_{FCop}}\right)} \quad (16)$$

The parameters used for the design of PEMFC system are given in Table 1, and its polarization curve is given in Fig. 3.

Table 1 PEM fuel cell stack design parameters

Parameters	Values
Rated power of fuel cell	6.0 kW
Maximum voltage of fuel cell (V_{MPP})	45 V
Maximum current of fuel cell (I_{MPP})	133.33A
Voltage of fuel cell at open circuit (V_{OC})	65 V
Partial pressure of oxygen	1 bar
Partial pressure of hydrogen	1.5 bar
Number fuel cells used (n)	65
Nominal air flowing rate (I_{pm})	506.4
Gasses constant (R)	84.092 [J.mol^{-1}.K^{-1}]
Faraday constant (F)	95,432.218 [C.mol^{-1}]
Oxidant composition	21%
Fuel composition	99.95%
Hydrogen utilization	99.56%
Utilization of oxygen	59.3%

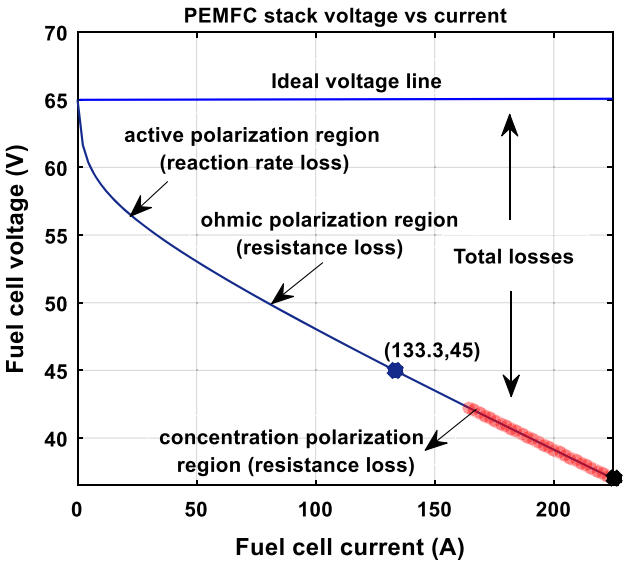

Fig. 3 PEM fuel cell voltage versus current characteristics

4 Design and analysis of MPPT Techniques

The working behavior of fuel cell is mainly depending on the parameters: hydrogen, oxygen, applied load variations, and fuel cell operating temperature. Here, the hybrid MPPT techniques are discussed and compared for improving the efficiency of PEM fuel cell stack at different working temperature conditions. The compared MPPT techniques are classified as VSS-P&O (Harrag and Rezk 2021), RBFN (Zhang and Wang 2018), FLC-VSSIC (Aly and Rezk 2020), FLC-IHC (Alajmi, et al. 2010), and IBeta-FLC-based MPPT techniques. The comparative analysis has been done in terms of steady-state oscillations across MPP,

maximum power output, sensing parameters, tracking speed, rising time of output power, and power conversion efficiency.

(a). VSS-P&O-based MPPT technique for fuel cell stack.

From the literature survey, the P&O is a most popular and conventional power point tracing technique because of its attractive features are easy to design and high simplicity. The major drawback of this technique is not suitable for diverse temperature conditions of PEMFC stack. In article (Harrag and Rezk 2021), a VSS-P&O is applied to trace the required peak power point of the fuel cell. Here, at starting, a high perturbation step is applied to the PEMFC in order to reach the operating point of fuel cell closer to the true MPP. Finally, less perturbation step size is used to find out the real MPP with high accuracy.

(b). RBFN-based MPPT technique for fuel cell stack.

From the literature survey (Zhang and Wang 2018), Artificial Neural Networks (ANN) are the information processing networks and which are used to design the computational complex systems. The ANN consist of multiple neurons and which are interconnected in the form of layers. At the time of training, the fuel stack information is distributed to all over the neurons in order to start the learning process of the network.

In article (Lin-Kwong-Chon, et al. 2019), a RBFN is used in neural network to trace the MPP of the fuel cell stack. The RBFN involving three layers which are input layer, middle layer, and production layer. The structure of RBFN is shown in Fig. 4. The fuel cell generated voltage (V_{FC}) and output current (I_{FC}) are given to RBFN input layer, and its output is given to the middle layer. The number of hidden layer neurons is chosen based on the realistic process. The training of RBFN has been done in two steps which are supervised learning and unsupervised learning. The unsupervised learning is functional to the input constraints and which are controlled by using radial

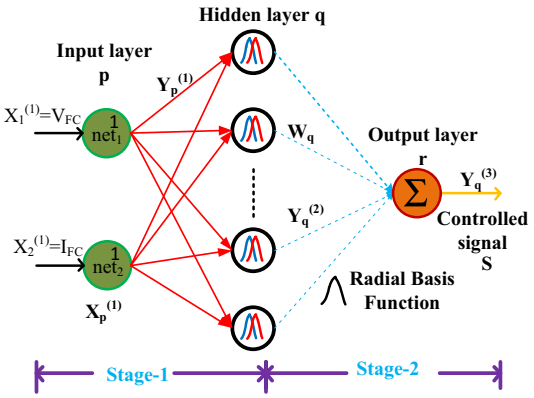

Fig. 4 Radial basic functional network MPPT controller, (Lin-Kwong-Chon, et al. 2019)

basic functions. From Fig. 4, the net input and output of an input layer is derived as follows:

$$\text{net}_p^{(1)} = x_p^1(k);\ k = 1,2 \tag{17}$$

$$y_p^{(1)}(k) = f_p^{(1)}(\text{net}_p^{(1)}(k)) = \text{net}_p^1(k);\ k = 1,2 \tag{18}$$

where x_p^1 indicates the input layer and it consist of a fuel cell output voltage $(x_1^1 = V_{FC})$, and output current $(x_2^1 = V_{FC})$. The input layer net and output are indicated as net_p^1 and y_p^1. Similar to the input layer, the net input and output of hidden layer are derived as follows:

$$\text{net}_q^{(2)}(k) = -(X - \mu_q)^T * \sum\nolimits_q (X - \mu_q) \tag{19}$$

$$y_q^{(2)}(k) = f_q^{(2)}(\text{net}_q^{(2)}(k)); q = 1,2,3,4,\ldots,k \tag{20}$$

The terms $\sum_q$ and μ_q are the Gaussian function and standard mean, respectively.

$$\sum\nolimits_q = \text{diag}\left[1/\sigma_{1q}^2 \quad 1/\sigma_{2q}^2 \quad .... \quad ... \quad 1/\sigma_{kq}^2 \right] \tag{21}$$

$$\mu_q = [\varepsilon_{1q} \quad \varepsilon_{2q} \quad .... \quad ... \quad \varepsilon_{kq}] \tag{22}$$

The final layer has a single neuron, and it gives a controlled output signal by using a linear activation function in order to generate the optimum duty cycle of the boost converter. The net and output of the final layer are derived as (Srinivasan, et al. 2021) follows:

$$\text{net}_r^{(3)} = \sum\nolimits_q W_q y_q^2(k); \quad k = 1,2,\ldots,n \tag{23}$$

$$y_r^{(3)}(k) = f_r^{(3)}((\text{net}_r^3(k)) = \text{net}_r^3(k) \tag{24}$$

The matrix form of the input (x) and output (y) signals is given to the RBFN controller, and their corresponding orders are 700 by 2 and 700 by 1.

$$[x] = [x_1 \quad x_2 \quad x_3 \quad ,\ldots,x_n] \tag{25}$$

$$[y] = [y_1 \quad y_2 \quad y_3 \quad ,\ldots,y_n] \tag{26}$$

The input layer process the entire inputs, and it gives a output which is derived as follows:

$$z = (x - x_{\min})\left(\frac{y_{\max} - y_{\min}}{x_{\max} - x_{\min}}\right) + y_{\min} \tag{27}$$

The bias (b) and weights (W) are determined by using a supervised learning. The output of the hidden and output layers are calculated as follows:

$$h = (zw + b) * \log(\text{sigmoid}) \tag{28}$$

$$z = (h - y_{\min})\left(\frac{y_{\max} - y_{\min}}{x_{\max} - x_{\min}}\right) + x_{\min} \tag{29}$$

The error signal of the output layer is derived as follows:

$$\text{error} = \sum \frac{1}{2}(V_{\text{dc-ref}} - V_{\text{MPP}}) \tag{30}$$

where $V_{\text{dc-ref}}$ is the required reference voltage and V_{MPP} is the peak voltage of fuel cell.

(c). FLC-VSSIC-based MPPT technique for fuel cell stack.

As discussed previously, the conventional fixed step size IC MPPT technique is having a drawback of high steady-state oscillations, less convergence speed, high settling time of MPP, less efficiency, and high implementation complexity (Harrag and Messalti 2018). In addition to that, it is not useful for dynamic temperature condition of fuel cell. In article (Aly and Rezk 2020), a fuzzy logic controller is used in order to decide and vary the step size of the IC MPPT technique. As a result, the tracking speed of the MPP is increased. The block diagram of FLC-based VSSIC MPPT controller is shown in Fig. 5.

From Fig. 5, the term dP_{FC} is defined as the variation of fuel cell output power which is calculated by multiplying the variation of fuel cell output voltage (dV_{FC}) and the current (dI_{FC}). The slope (S_{P}) of V-I curve and old step value ($S_{\text{T-old}}$) are the inputs to the fuzzy controller, and its output is the new step value ($S_{\text{T-new}}$) which is given to the IC technique in order to obtain the optimum duty cycle of the boost converter. The FLC consist of three fuzzy subsets (small, medium, and large), and nine rules which are shown in Figs. 6 and 7. The fuzzy rules are formed to minimize the slope of the V-I curve.

Here, the Mamdani's max–min combination is used to decide the step size of IC technique. If the operating point of the PEMFC stack is at the left side of MPP, then the duty cycle of the SSUIBC is updated by using Eq. (31). Otherwise, Eq. (33) is used to adjust the duty value of the boost converter.

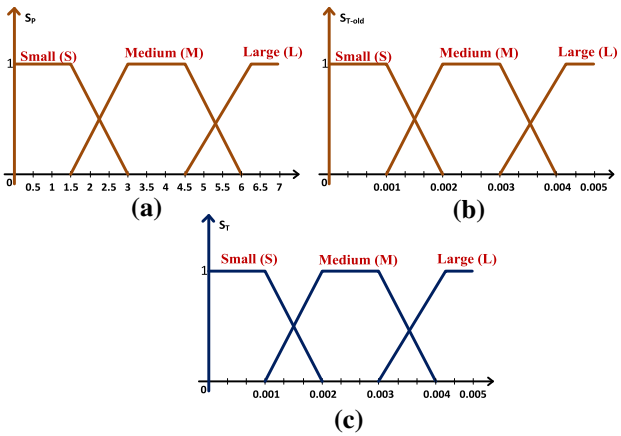

Fig. 6 Membership functions of FLC, **a** Input slope (S_{P}), **b** Input old step ($S_{\text{T-old}}$), and **c**. Output new step ($S_{\text{T-new}}$)

$$\begin{cases} \text{if } S_p \text{ is small } \& S_{T-old} \text{ is small than } \Delta S_T \text{ is small} \\ \text{if } S_p \text{ is small } \& S_{T-old} \text{ is medium than } \Delta S_T \text{ is small} \\ \text{if } S_p \text{ is small } \& S_{T-old} \text{ is large than } \Delta S_T \text{ is small} \\ \text{if } S_p \text{ is medium } \& S_{T-old} \text{ is small than } \Delta S_T \text{ is small} \\ \text{if } S_p \text{ is medium } \& S_{T-old} \text{ is medium than } \Delta S_T \text{ is medium} \\ \text{if } S_p \text{ is medium } \& S_{T-old} \text{ is large than } \Delta S_T \text{ is large} \\ \text{if } S_p \text{ is large } \& S_{T-old} \text{ is large than } \Delta S_T \text{ is large} \\ \text{if } S_p \text{ is large } \& S_{T-old} \text{ is medium than } \Delta S_T \text{ is large} \\ \text{if } S_p \text{ is large } \& S_{T-old} \text{ is small than } \Delta S_T \text{ is medium} \end{cases}$$

Fig. 7 FLC rules for VSSIC MPPT technique

$$D(k) = D(k-1) + S_{\text{T-new}} * \text{sig}\left(\frac{\Delta I}{\Delta V} + \frac{I}{V}\right) \tag{31}$$

where

$$S_{T-new} = N * \frac{\Delta P}{\Delta V}; \quad S_P = \frac{\Delta P}{\Delta V} = \frac{P(k) - P(k-1)}{V(k) - V(k-1)} \tag{32}$$

$$D(k) = D(k-1) - S_{\text{T-new}} * \text{sig}\left(\frac{\Delta I}{\Delta V} + \frac{I}{V}\right) \tag{33}$$

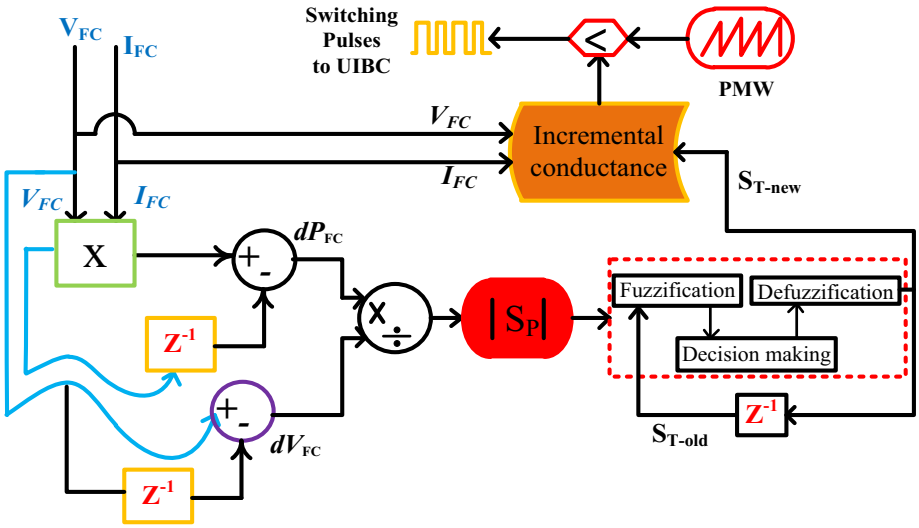

Fig. 5 FLC-based VSSIC MPPT controller for PEMFC stack system

$$\left.\begin{array}{l} if\ \Delta P > 0 \\ if\ \Delta I > 0 \\ D(x) = D(x-1) \\ \quad +\Delta D \\ else \\ D(x) = D(x-1) \\ \quad -\Delta D \\ end \end{array}\right\} => \left\{\begin{array}{l} if\ \Delta I\ is\ PB\ and\ \Delta P\ is\ PB\ then\ \Delta D\ is\ PB \\ if\ \Delta I\ is\ PS\ and\ \Delta P\ is\ PB\ then\ \Delta D\ is\ PB \\ if\ \Delta I\ is\ NB\ and\ \Delta P\ is\ PB\ then\ \Delta D\ is\ NB \\ if\ \Delta I\ is\ NS\ and\ \Delta P\ is\ PB\ then\ \Delta D\ is\ NB \\ if\ \Delta I\ is\ PB\ and\ \Delta P\ is\ PS\ then\ \Delta D\ is\ PS \\ if\ \Delta I\ is\ PS\ and\ \Delta P\ is\ PS\ then\ \Delta D\ is\ PS \\ if\ \Delta I\ is\ NB\ and\ \Delta P\ is\ PS\ then\ \Delta D\ is\ NS \\ if\ \Delta I\ is\ PB\ and\ \Delta P\ is\ PS\ then\ \Delta D\ is\ NS \end{array}\right.$$

$$\left.\begin{array}{l} elseif\ \Delta P < 0 \\ if\ \Delta I > 0 \\ D(x) = D(x-1) \\ \quad -\Delta D \\ else \\ D(x) = D(x-1) \\ \quad +\Delta D \\ end \end{array}\right\} => \left\{\begin{array}{l} if\ \Delta I\ is\ PB\ and\ \Delta P\ is\ NB\ then\ \Delta D\ is\ NB \\ if \Delta I\ is\ PS\ and\ \Delta P\ is\ NB\ then\ \Delta D\ is\ NB \\ if\ \Delta I\ is\ NB\ and\ \Delta P\ is\ NB\ then\ \Delta D\ is\ PB \\ if\ \Delta I\ is\ NS\ and\ \Delta P\ is\ NB\ then\ \Delta D\ is\ PB \\ if\ \Delta I\ is\ PB\ and\ \Delta P\ is\ PS\ then\ \Delta D\ is\ NS \\ if\ \Delta I\ is\ PS\ and\ \Delta P\ is\ PS\ then\ \Delta D\ is\ NS \\ if\ \Delta I\ is\ NB\ and\ \Delta P\ is\ PS\ then\ \Delta D\ is\ PS \\ if\ \Delta I\ is\ PS\ and\ \Delta P\ is\ PS\ then\ \Delta D\ is\ PS \end{array}\right.$$

Fig. 8 Fuzzification rules of improved HC MPPT controller

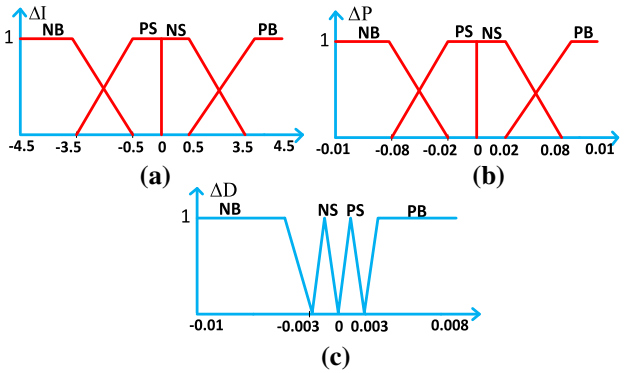

Fig. 9 Membership functions of, **a** Fuel cell current, **b** Voltage, and **c** Duty cycle

where $D\ (k)$ and $D\ (k\text{-}1)$ are the present and existed duty cycles of the universal input voltage boost converter. The term 'N' indicates the scaling factor. At starting, the selected scaling factor value is high in order to reduce the tracing time of MPP and finally small step value is considered to suppress the steady-state oscillations across the MPP.

(d). FLC- IHC MPPT technique for fuel cell stack.

The drawbacks of HC MPPT technique are overcome by using an FLC-IHC technique. Here, the fuzzy logic controller is used to improve the searching mechanism of HC MPPT technique. The advantages of the hybrid MPPT technique are high convergence speed, less settling time, and high accuracy when compare to the conventional HC method (Alajmi, et al. 2010). The block diagram of FLC-IHC technique is shown in Fig. 8. The PEMFC stack power (P_{FC}) and currents (I_{FC}) are the inputs to the FLC, and its output is controlled duty cycle.

$$\Delta P = P(i) - P(i-1) \tag{34}$$

$$\Delta I = I(i) - I(i-1) \tag{35}$$

$$\Delta D = D(i) - D(i-1) \tag{36}$$

where ΔP, ΔI, and ΔD are the change of fuel output power, current and converter duty cycle. Here, the operating point of PEMFC is not coincide with the true MPP at diverse temperature conditions. So,ΔP is flows through the gain controller to reverse its direction. The FLC inputs and output are transferred into four fuzzy subsets which are Positive Big (PB), Negative Big (NB), Positive Small (PS), and Negative Small (NS). Based on four fuzzy sets, the FLC consist of sixteen fuzzy rules and which are formed based on the controlling of HC technique. The Mamdani's Max–min technique is used for the operation of fuzzy combination. The fuzzification of IHC rules is given in Fig. 8, and the membership functions of fuel cell output power, current, and duty cycle are shown in Fig. 9a, b and c.

(e). Proposed IBeta-FLC MPPT technique for fuel cell stack.

The major drawback of fuzzy logic controller is required high knowledge person for training its complicated rules. In order to overcome the drawback of this basic fuzzy technique, a hybrid (IBeta-based FLC) MPPT technique is proposed to improve the dynamic response of the fuel cell stack. Here, beta (β) is varied instead of varying fuel cell output voltage and power. The variable β is given to the FLC in order to operate the PEMFC fed boost converter system at dynamic temperature conditions. In addition to that, the β is used to optimize the number of fuzzy rules.

Here, the Mamdani's, Max–min, and center of gravity techniques are used for fuzzy interference, fuzzy combination, and defuzzification, respectively. The block diagram of hybrid MPPT controller is shown in Fig. 10.

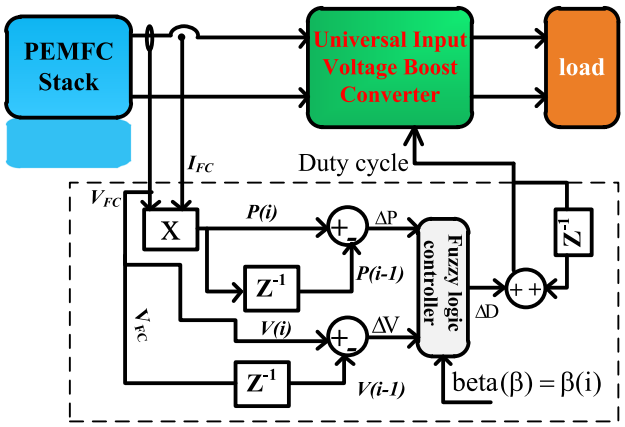

Fig. 10 Block diagram of proposed MPPT controller

$$\beta(i) = \log\left(\frac{I_{FC}}{V_{FC}}\right) - n * V_{FC} \quad (37)$$

where V_{FC} and I_{FC} are fuel cell voltage and current. The term 'n' indicates the total number of cells in the PEMFC stack. Based on different operating conditions of PEMFC stack, the parameter β is divided into three parts (β_{min}, β_{max}, and β_{mode}) which are varied continuously until obtaining the optimum value of beta parameter. If the determined beta value is within the range, then the operating point of fuel cell is nearer to the MPP. After that, the FLC is used to suppress the oscillations of MPP. The fuzzy controller membership functions are shown in Fig. 11. From Fig. 11, the formation fuzzy rules are given in Table 2.

From Table 2, the output is PB at minimum beta value and it is NB at maximum beta value. The maximum possible fuzzy sets at moderate beta value are PS, NS, and ZE.

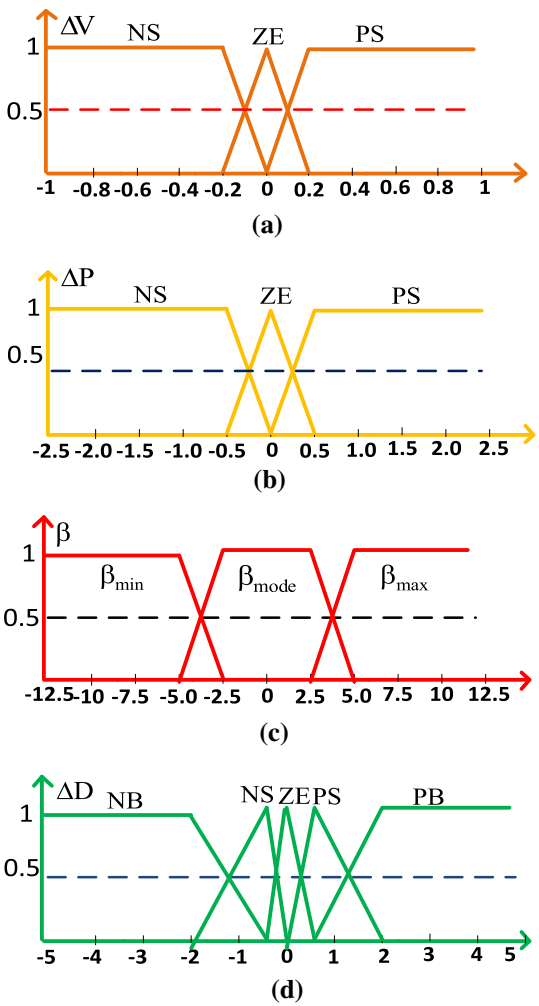

Fig. 11 Membership functions of, **a** Fuel cell voltage, **b** Power, **c** beta parameter, and **d** Duty cycle of boost converter

Table 2 Fuzzy rules of the proposed MPPT technique

β_{max}	NB			
β_{mode}	PS	PS	ZE	NS
	ZE	ZE	ZE	ZE
	NS	NS	ZE	PS
	$\Delta V/\Delta P$	NS	ZE	PS
β_{min}	PB			

5 Design and analysis of SSUIBC

The universal input voltage, high step-up, and transformerless boost converter consist of four semiconductor devices which are classified as three diodes (D_x, D_y, and D_z), and one Metal Oxide Field Effect Transistor (MOSFET) switch (Q). In addition, it consists of four capacitors (C_x, C_y, C_z, and C_a), three inductors (L_x, L_y, and L_z), and one resistor (R_0). The elements C_x, L_x, Q, and D_x act as a conventional boost switching converter and the components D_y, D_z, L_x, L_y, C_y, and C_a, and C_z are formed as a filter network (see in Fig. 1) and it is interfaced in between the conventional converter and output capacitor (C_0).

The interfacing network is useful for improving the output voltage profile of the fuel stack. In addition, it reduces the voltage stress across the diodes and switch. Based on the switching behavior of MOSFET, the proposed converter works in three modes of operations (see in Table 3).

6 Switching state: I

The first switching state of the converter is shown in Fig. 12a. From Fig. 12a, the output voltage and currents of fuel cell are defined as V_{FC}, and I_{FC}. The instantaneous voltages across the capacitors (C_x, C_y, C_z, C_0, and C_a) and inductors (L_x, L_y, and L_z) are V_{Cx}, V_{Cy}, V_{Cz}, V_{C0}, V_{Ca}, V_{Lx}, V_{Ly}, and V_{Lz}, respectively. Similarly, the current flowing through the capacitors and inductors are I_{Cx}, I_{Cy}, I_{Cz}, I_{C0}, I_{Ca}, I_{Lx}, I_{Ly}, and I_{Lz}, respectively. The charging and discharging currents of the capacitors are $I_{Cx\text{-}chg}$, $I_{Cy\text{-}chg}$, $I_{Cz\text{-}chg}$, $I_{C0\text{-}chg}$, $I_{Ca\text{-}chg}$, $I_{Cx\text{-}disg}$, $I_{Cy\text{-}disg}$, $I_{Cz\text{-}disg}$, $I_{C0\text{-}disg}$ and $I_{Ca\text{-}disg}$, respectively. Here, there are three assumptions have been considered to analyze the CCM, and DCM of operation of the boost converter. The first assumption is, all the semiconductor switches are in ideal condition, and second one is, the equivalent series resistance of the inductors plus capacitors are zero. Finally, the third assumption is the selection of capacitors and inductors are high in order to run the converter at CCM of operation.

Table 3 Switching behavior of UIVBC

	State-I (CCM and DCM)	State-II (CCM and DCM)	State-III (DCM)
Q	ON condition	OFF condition	OFF condition
D_X	OFF condition	ON condition	OFF condition
D_Y	OFF condition	ON condition	OFF condition
D_Z	OFF condition	ON condition	OFF condition

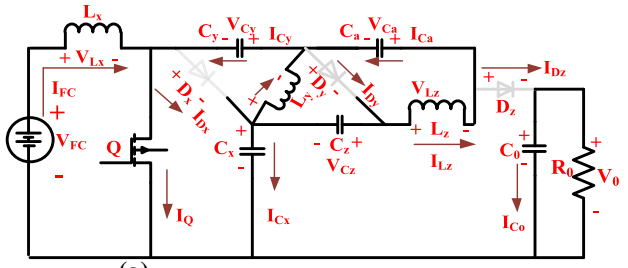

(a) Block diagram of SSUIBC at first switching state

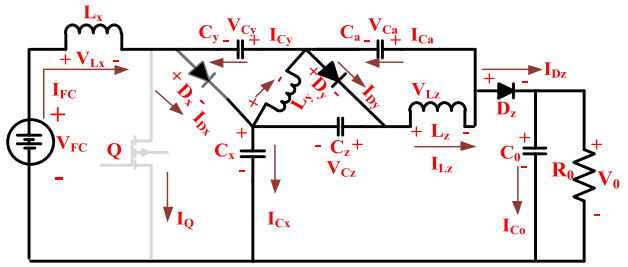

(b) Block diagram of SSUIBC at second switching state

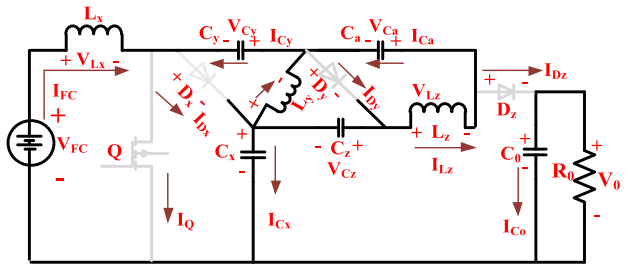

(c) Block diagram of SSUIBC at third switching state

Fig. 12 **a** Block diagram of SSUIBC at first switching state. **b** Block diagram of SSUIBC at second switching state. **c** Block diagram of SSUIBC at third switching state

In the first switching state, the voltage across the gate to source terminals of the MOSFET is extreme then the power converter starts working in CCM and DCM of actions. When the switch (Q) is in conduction state, then the diodes (D_x, D_y, and D_z) are in OFF state and capacitors, C_y and C_a, starts charging, and C_x, C_z, and C_0 starts discharging as shown in Fig. 12a. The current flowing through the five capacitors (refer Eq. 38) and voltage across the three inductors (refer Eq. 39) are derived by using Kirchhoff's Current Law and Kirchhoff's Voltage Law.

$$\begin{cases} I_{\mathrm{Cy-chg}} = I_{\mathrm{Cx-disg}} = I_{Ly} + I_{Lz} \\ I_{\mathrm{Cz-disg}} = I_{\mathrm{Ca-chg}} = I_{Lz} \\ I_{\mathrm{C0-disg}} = I_0 \end{cases} \tag{38}$$

$$\begin{cases} V_{Lx} = V_{FC} \\ V_{Ly} = V_{Cx} - V_{Cy} \\ V_{Lz} = V_{Cx} + V_{Cz} - V_{Ca} - V_{Cy} \end{cases} \tag{39}$$

6.1 Switching state: II

In this switching state, the voltage (V_{gs}) across the gate to source is very low. As result, the switch (Q) is in blocking state and the diodes (D_x, D_y, and D_z) are in conduction state. The converter works in both the modes of operation as given in Fig. 12b. From Fig. 12b, the capacitors C_y and C_a starts discharging and the capacitors C_x, C_z and C_0 starts charging.

The Kirchhoff's Current and the Kirchhoff's Voltage Laws are applied to the converter in order to derive the current flowing through the inductors and voltage across the capacitors.

$$\begin{cases} I_{\mathrm{Cy-disg}} = I_{\mathrm{Ca-disg}} + I_{Lz} + I_{\mathrm{Lz-chg}} - I_{Ly} \\ I_{\mathrm{Cx-chg}} = -I_{\mathrm{Cy-disg}} + I_{Lx} - I_{Ly} + I_{\mathrm{Cz-chg}} \\ I_{\mathrm{C0-chg}} = I_{\mathrm{Ca-disg}} + I_{Lz} - I_0 \end{cases} \tag{40}$$

$$\begin{cases} V_{Lx} = V_{FC} \\ V_{Ly} = -V_{Cy} = -V_{Cz} \\ V_{Lz} = V_{Cx} + V_{Cz} - V_{Ca} - V_{Cy} \end{cases} \tag{41}$$

6.2 Switching state: III

In this switching state, the converter works in DCM of operation. Here, the voltage across the gate to source terminal is very low. As a result, all the semiconductors devices are in reverse biased state as illustrated in Fig. 12c.

From Fig. 12c, the constant current flowing through the inductors (L_x, L_y, and L_z) are $I_{\mathrm{Lx\text{-}min}}$, $I_{\mathrm{Ly\text{-}min}}$, and $I_{\mathrm{Lz\text{-}min}}$ and its summation is zero. In addition, the voltage across each inductor is zero which is given in Eq. (43).

$$I_{Lx-\min} + I_{Ly-\min} + I_{Lz-\min} = 0 \tag{42}$$

$$V_{Lx} = V_{Ly} = V_{Lz} = 0 \tag{43}$$

(a). Steady-state behavior of boost converter under CCM of operation.

Here, the switching state-I and switching state-II are used to analyze the CCM of operation of the boost converter. From Fig. 12a and Eqs (39) and (41), the voltage gain of proposed boost converter is derived as follows:

$$V_{Cy} = V_{Ca} = V_{Cz} = \frac{D}{(1-D)} V_{FC} \tag{44}$$

$$V_{Cx} = \frac{1}{(1-D)} V_{FC} \tag{45}$$

$$V_0 = \frac{1+2D}{1-D} V_{FC} \tag{46}$$

$$Gain_{CCM} = \frac{V_0}{V_{FC}} = \frac{1+2D}{1-D} \tag{47}$$

From Fig. 12a, the voltage stress across the power semiconductors is equal to V_{Cx}. Eqs (38)-(41) are used to derive the voltage stress across the diodes (V_D) switch (V_Q).

$$\begin{cases} V_D = V_Q = V_{FC} * \dfrac{1}{1-D} V_{Cx} \\ V_{Dx} = V_{Dy} = V_{Dz} = V_D \end{cases} \tag{48}$$

Eqs (46), and (47) are used to derive the voltage stress across the switch in terms voltage gain.

$$V_D = V_Q = \frac{2 + \text{Gain}_{\text{CCM}}}{3 * \text{Gain}_{\text{CCM}}} * V_0 \tag{49}$$

The current stress across each inductor is obtained by considering the generated converter power ($P_0 = V_0 * I_0$) is equal to the fuel cell power ($P_{FC} = V_{FC} * I_{FC}$).

$$I_{Ly} = I_{Lz} = I_0 \tag{50}$$

$$I_{Lx} = \frac{1+2D}{1-D} I_0 = \text{Gain}_{\text{CCM}} I_0 \tag{51}$$

The charge-second balance principle is applied to each capacitor in order to derive their charging and discharging currents.

$$\begin{cases} I_{\text{Cy-chg}} = 2I_0 \\ I_{\text{Cy-disg}} = 2I_0 \dfrac{D}{1-D} = \dfrac{\text{Gain}_{\text{CCM}} - 1}{3} 2I_0 \end{cases} \tag{52}$$

$$\begin{cases} I_{\text{Ca-chg}} = I_0 \\ I_{\text{Ca-disg}} = I_0 \dfrac{D}{1-D} = \dfrac{\text{Gain}_{\text{CCM}} - 1}{3} I_0 \end{cases} \tag{53}$$

$$\begin{cases} I_{\text{Cz-chg}} = 2I_0 \dfrac{D}{1-D} = 2I_0 \dfrac{\text{Gain}_{\text{CCM}} - 1}{3} \\ I_{\text{Cz\_disg}} = 2I_0 \end{cases} \tag{54}$$

$$\begin{cases} I_{\text{Cx-chg}} = I_0 \dfrac{D}{1-D} = \dfrac{\text{Gain}_{\text{CCM}} - 1}{3} I_0 \\ I_{\text{Cx-disg}} = I_0 \end{cases} \tag{55}$$

$$\begin{cases} I_{\text{C0-chg}} = I_0 \dfrac{D}{1-D} = \dfrac{\text{Gain}_{\text{CCM}} - 1}{3} I_0 \\ I_{\text{C0-disg}} = I_0 \end{cases} \tag{56}$$

From Fig. 12b and c, the currents passing over the power diodes plus the switch are calculated as follows:

$$I_Q = I_{Lx} + I_{Ly} + I_{Lz} = I_0 \frac{3}{1-D} \tag{57}$$

$$I_{Dx} = I_{Lx} - I_{\text{Cy\_disg}} = I_0 \frac{1}{1-D} \tag{58}$$

$$I_{Dy} = I_{Ly} + I_{\text{Cy-chg}} - I_{\text{Ca-disg}} = I_0 \frac{1}{1-D} \tag{59}$$

$$I_{Dz} = I_{\text{Ca-disg}} = I_0 \left(1 - \frac{3}{1-D}\right) \tag{60}$$

By using Eqs (51), and (57)–(60), the current stress across the switch is obtained as follows:

$$I_Q = (\text{Gain}_{\text{CCM}} + 2) I_0 \tag{61}$$

$$I_{Dx} = I_{Dy} = I_{Dz} = \left(\frac{\text{Gain}_{\text{CCM}} + 2}{3}\right) I_0 \tag{62}$$

The RMS currents flowing through the semiconductor devices and capacitors are derived as follows:

$$I_{Q_{\text{RMS}}} = \sqrt{(\text{Gain}_{\text{CCM}} + 2) * (\text{Gain}_{\text{CCM}} - 1)} * I_0 \tag{63}$$

$$I_{\text{Dx-RMS}} = I_{\text{Dy-RMS}} = I_{\text{Dz-RMS}} = \sqrt{\frac{\text{Gain}_{\text{CCM}} + 2}{3}} * I_0 \tag{64}$$

$$I_{\text{Cy-RMS}} = I_{\text{Cx-RMS}} = \sqrt[2]{\frac{\text{Gain}_{\text{CCM}} - 1}{3}} * I_0 \tag{65}$$

$$I_{\text{Cz-RMS}} = I_{\text{Ca-RMS}} = I_{\text{C0-RMS}} = \sqrt{\frac{\text{Gain}_{\text{CCM}} - 1}{3}} * I_0 \tag{66}$$

(i). Internal resistance effect on voltage gain.

The active and passive components of the proposed converter consist of internal resistances which are affect the boost converter voltage profile. The non-ideal model proposed universal input voltage, high step-up boost converter is given in Fig. 13. From Fig. 13, the internal

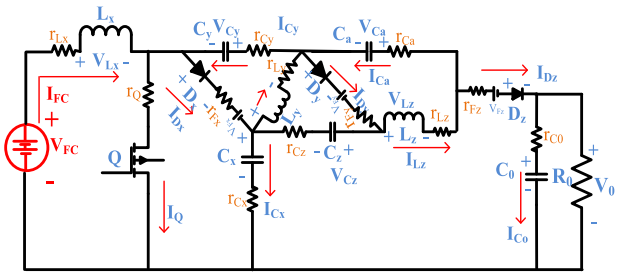

Fig. 13 Internal resistances effect on voltage gain

resistances of the all inductors are same ($r_{Lx} = r_{Ly} = r_{Lz} = r_L$) and all capacitors internal resistances are same ($r_{Cx} = r_{Cy} = r_{Cz} = r_{C0} = r_C$). Similarly, the forward voltage drop across the three diodes are same ($V_{Fx} = V_{Fy} = V_{Fz} = V_F$) and their corresponding internal resistances are same ($r_{Fx} = r_{Fy} = r_{Fz} = r_F$). The MOSFET conduction resistance is indicated as r_Q.

By considering the internal resistances of active and passive elements, the modified voltage gain of the proposed converter is given in Eq. (67).

(b). Analysis of proposed converter under DCM of operation.

Here, the switching state-I, II and III are used to analyze the DCM of operation. From Eqs (44)–(47), the voltage gain of dc-dc converter is evaluated as follows:

$$\text{Gain}_{\text{CCM}} = \frac{R_0(1-D) * (V_{FC} - 3V_F + 3DV_F + 2DV_{FC})}{V_{FC}(R_0 + 3r_F + 3r_L + D(6r_C - 2R_0 - 3r_D + 3r_Q + D(R_0 - 6r_C + 6r_L - 12r_Q)))} \tag{67}$$

$$V_{Cy} = V_{Ca} = V_{Cz} = \frac{V_0 - V_{\text{in}}}{3} \tag{68}$$

$$V_{Cx} = V_{\text{FC}} + V_{Ca} = \frac{V_0 + 2V_{\text{FC}}}{3} \tag{69}$$

$$V_0 = V_{Cx} + 2V_{Ca} \tag{70}$$

By considering Eqs (38), (40), (42), the voltage-second working principle is applied on L_x in order to determine the boost converter voltage gain at discontinuous mode.

$$\frac{1}{T}\left(\int_0^{dt} V_{FC} * \mathrm{d}t - \int_0^{d_x t} \frac{(V_0 - V_{FC})}{3} * \mathrm{d}t\right) = 0 \tag{71}$$

From Eq. (51), the variable d_x is required in order to derive the voltage gain of SSUIBC. From Eqs. (57)–(60), the current passing through the switch is equal to the summation of inductor currents and the current passing through the diode is equal to the one third of the inductor currents. The peak currents of the inductors and diodes are derived as follows:

$$\begin{cases} \Delta I_{Lx} = \dfrac{DV_{\text{FC}}}{f_s L_x} \\ \Delta I_{Ly} = \dfrac{DV_{\text{FC}}}{f_s L_y} \\ \Delta I_{Lz} = \dfrac{DV_{\text{FC}}}{f_s L_z} \end{cases} \tag{72}$$

$$I_{\text{Dpeak}} = \frac{1}{3}\left(\Delta I_{Lx} + \Delta I_{Ly} + \Delta I_{Lz}\right) \tag{73}$$

From Eqs. (71) and (72), the peak diode current is rewritten as follows:

$$I_{\text{Dpeak}} = \frac{D * V_{\text{FC}}}{3 f_s L_{\text{eq}}} \tag{74}$$

The average current flowing through each diode is equal to I_0.

$$\frac{1}{2} D_x I_{\text{Dpeak}} = \frac{V_0}{R} \tag{75}$$

By substituting Eq. (75) in Eq. (74), the term D_x is derived as follows:

$$D_x = \frac{6V_0}{D * V_{\text{FC}}}\tau \tag{76}$$

where τ is the time constant of the inductor. By substituting Eq. (75) in Eq. (70), then the voltage gain of the converter under DCM is derived as follows:

$$\text{Gain}_{\text{DCM}} = \frac{1}{2}\left(1 + \sqrt{1 + \frac{2D^2}{\tau}}\right) \tag{77}$$

(c). Boundary conditions of the proposed converter.

Here, the voltage gain of proposed converter is equal under CCM and DCM of operations. From Eqs. (46) and (76), the time constant of the inductor is derived as follows:

$$\tau_{\text{boun}} = \frac{D * (1-D)}{12D + 6} \tag{78}$$

If the time constant $\tau > \tau_{\text{boun}}$, then the proposed converter works in CCM of operation.

(d). Comparative analysis of non-isolated boost converters.

Here, the universal input voltage boost converter is analyzed along with the other dc-dc converters in terms of number of semiconductor devices that are utilized to implement the converter and voltage stress across the diodes and switch. The detailed comparison of transformer less boost converters is given in Table 4.

Table 4 Comparative analysis of non-isolated high step-up DC-DC boost converters

DC-DC converter	Voltage gain of the converter	Required diodes & switches	Capacitors & inductors	Voltage Stress on MOSFET	Voltage Stress on Diode	Design cost of the converter	Power conversion efficiency
BBC (Kaur, et al. 2017)	$\frac{1}{1-D}$	One diode One switch	One capacitor One inductor	1	1	Normal	Moderate
ETBC (Uthirasamy, et al. 2020)	$\frac{1}{D*(1-D)}$	Three diodes Two switches	Two capacitors Two inductors	$\frac{1}{2}+\sqrt{\frac{1}{4}-\frac{1}{g_{CCM}}}$	$\frac{3}{2}+\sqrt{\frac{1}{4}-\frac{1}{g_{CCM}}}$	Moderate	Less
SSVLBC (Ahmad 2020)	$\frac{1+D}{1-D}$	Three diodes One switch	Three capacitors Two inductors	$\frac{1+Gain_{CCM}}{2Gain_{CCM}}$	$\frac{1+Gain_{CCM}}{2Gain_{CCM}}$	High	NA
LICQBC (Li, et al. 2020a)	$\frac{1}{(1-D)(1+D)}$	Three diodes One switch	Two capacitors Two inductors	1	1	Moderate	High
HSTBC (Sadaghati, et al. 2020)	$\frac{2}{1-D}$	Two diodes Two switches	Two capacitors Two inductors	$\frac{1}{2}$	$\frac{1}{2}$	Less	Moderate
CPMBC (Li, et al. 2020b)	$\frac{2+D}{1-D}$	Three diodes Two witches	Three capacitors Three inductors	$\frac{1}{2}$	$\frac{1}{2}$	High	NA
NSHSBC (Hasanpour, et al. 2020)	$\frac{3-D}{1-D}$	Four diodes One switch	Four capacitors One inductor	$\frac{Gain_{CCM}-1}{2Gain_{CCM}}$	$\frac{Gain_{CCM}-1}{2Gain_{CCM}}$	Very High	Moderate
SSUIBC	$\frac{1+2D}{1-D}$	Three diodes One switch	Five capacitors Three inductors	$\frac{Gain_{CCM}+2}{3*Gain_{CCM}}$	$\frac{Gain_{CCM}+2}{3Gain_{CCM}}$	Moderate	High

7 Discussion of simulation results

Here, the major contribution of the work is design of the SSUIBC and it is used to step-up the fuel cell output voltage. As discussed previously, the SSUIBC converter is designed by interfacing a network in between the basic boost converter and load. The selected basic boost converter parameters are input inductor (L_x = 1.21 mH), output capacitor (C_0 = 300 µF), and load resistor (R_0 = 40 Ω). The added network capacitors ($C_y = C_z = C_a = C_x$) and inductors ($L_y = L_z$) values are 90 µF and 0.813 mH, respectively. From the block diagram (Fig. 1), the inductor L_x is used to suppress the low order distortions of PEMFC output voltage and C_0 is used to supply a constant voltage to the load. The fuel cell gives nonlinear voltage versus current characteristics. As a result, the maximum power extraction from the fuel cell is very difficult. In addition, the V-I curve consists of unique MPP and it varies based on the operating temperature conditions of PEMFC. Here, an IBeta-FLC is used to trace the peak power point of PEMFC and it is compared with other MPPT techniques at static temperature conditions.

(a). Static operating temperature condition of PEMFC (320 K).

The instantaneous PEMFC current and voltage are taken as inputs to the proposed MPPT controller, and its output is duty cycle. At static operating temperature condition, the PEMFC current and voltage by applying different MPPT techniques are given in Fig. 14a and b. Similarly, the converter operating duty cycle, output current, output voltage, output power by applying diverse power point tracing techniques are shown in Fig. 14c, d, e, and f. From Fig. 14a and b, the extracted PEMFC output current and voltage of VSS-P&O and RBFN-based MPPT techniques are 112.5A, 39.37 V, 113.2A, and 40.60 V, respectively. Similarly, the fuel cell current and voltage of FLC-IHC and FLC-VSSIC-based MPPT techniques are 112.8A, 42.60 V, 113.7A, and 42.02 V, respectively. The rising and settling

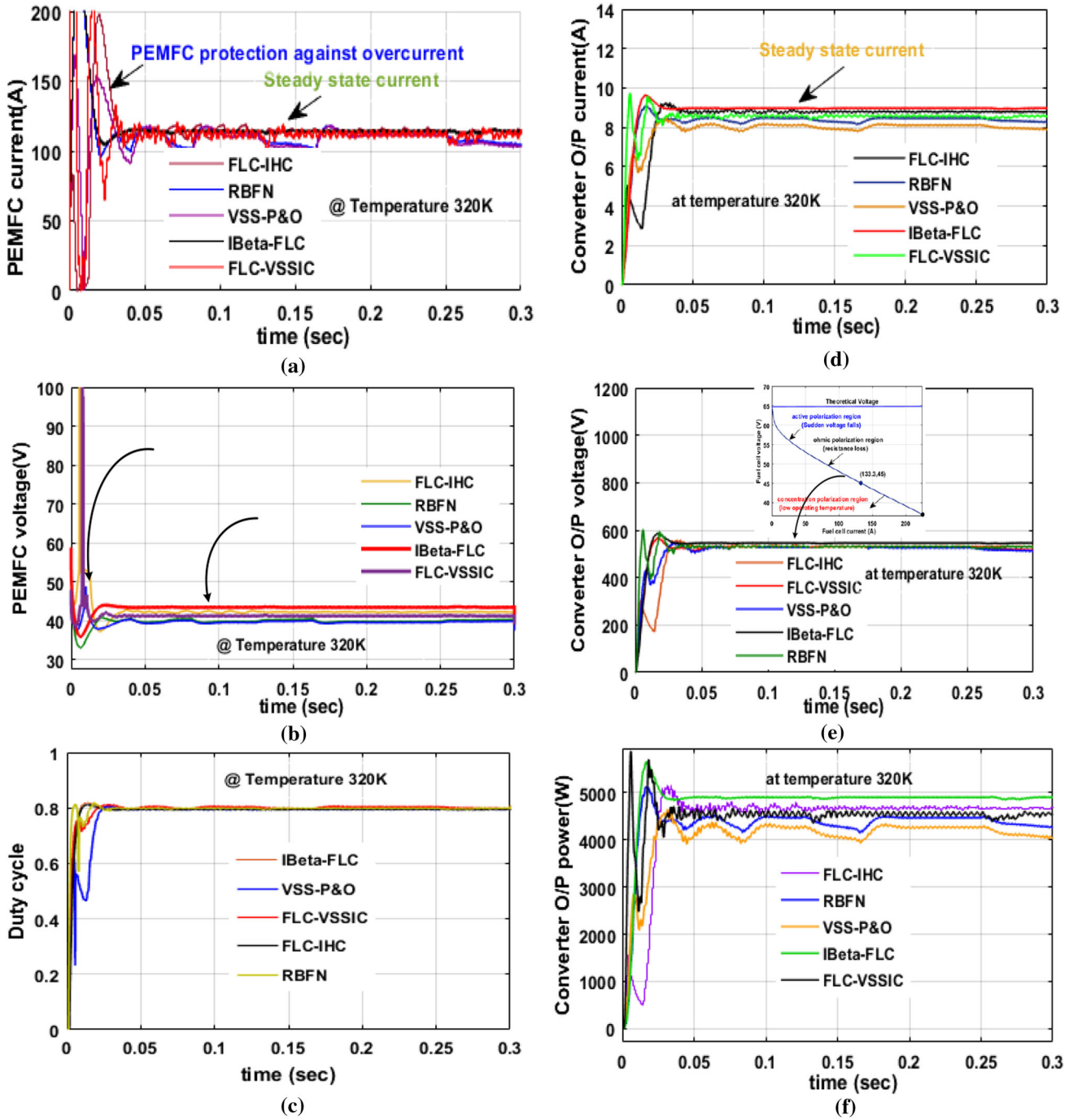

Fig. 14 **a** PEMFC current, **b** PEMFC voltage, **c** Duty cycle, **d** Converter O/P current, **e** Converter O/P voltage, **f** Converter O/P power at static temperature condition

of time of PEMFC output voltage by applying RBFN and an IBeta-FLC are 0.015 s, 0.041 s, 0.010 s, and 0.18 s, respectively.

The VSS-P&O, FLC-IHC, and FLC-VSSIC power point tracking controller gives the required duty cycle (0.79, 0.808, and 0.798) to the SSUIBC in order to improve the voltage profile of the fuel cell stack. From Fig. 14c, the fuel cell fed SSUIBC duty cycle by using IBeta-FLC is 0.793 which is less than the FLC-IHC. From Fig. 14d, e, and f, the converter output current, output voltage, and output power of RBFN and FLC-VSSIC-based power point tracking controller are 8.460A, 528.50 V, 4471.2 W, 8.751A, 531.522 V, and 4650.82 W, respectively. Similarly, the converter output voltage and output power of VSS-P&O, FLC-IHC, and IBeta-FLC-based controllers are 526.40 V, 4269.16 W, 533.61 V, 4716.49 W, 538.88 V,

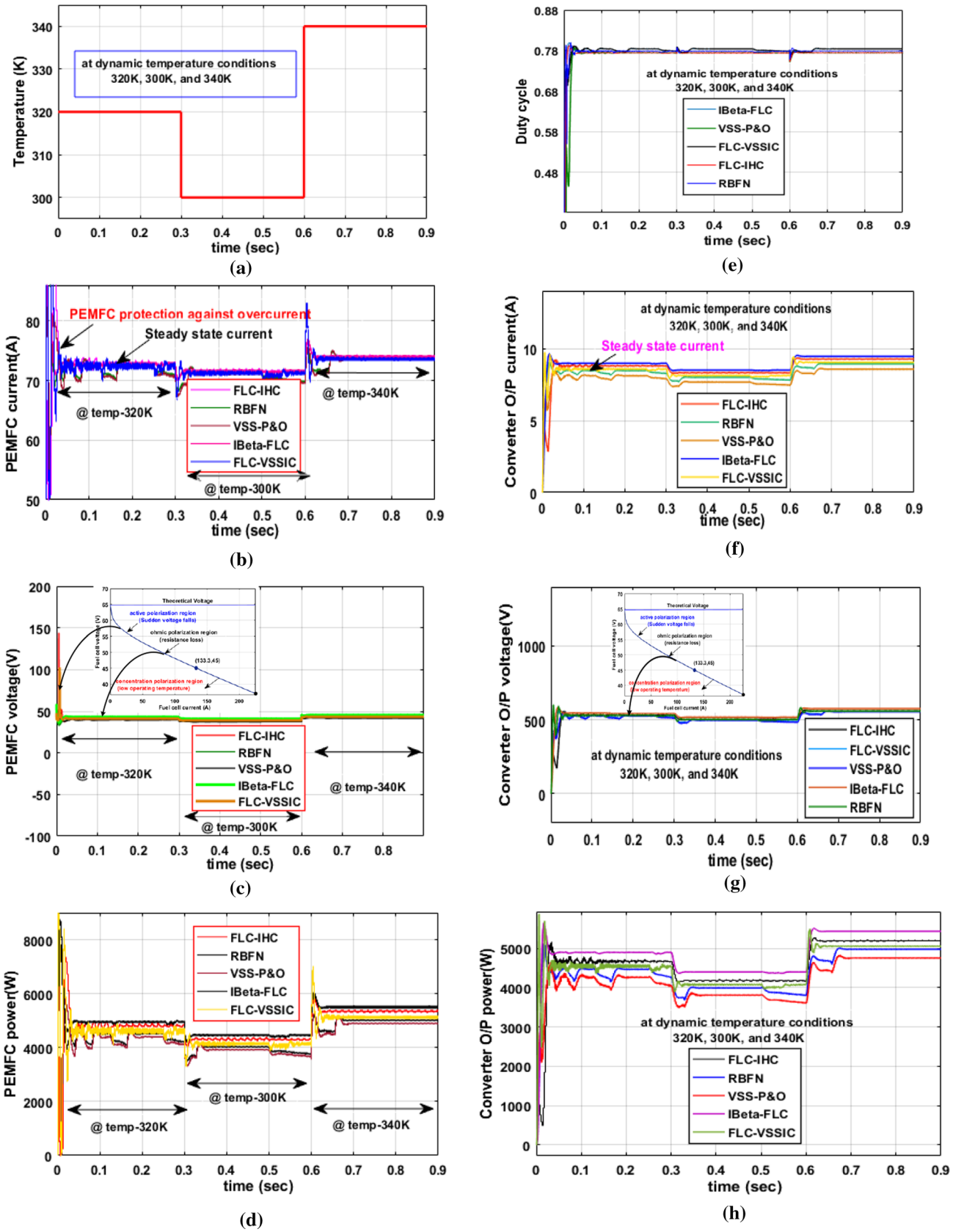

Fig. 15 **a** Variation of temperature. **b** PEMFC current. **c** PEMFC voltage. **d** PEMFC power. **e** Duty cycle. **f** Converter O/P current. **g** Converter O/P voltage. **h** Converter O/P power at dynamic temperature condition

Table 5 Performance parameters of PEMFC fed SSUIBC by applying different MPPT techniques

MPPT Technique	PEMFC current	PEMFC voltage	PEMFC power	Converter O/P current	Converter O/P voltage	Converter O/P power	efficiency	Settling time	Depends on PV	Oscillations	Complexity
Operating Temperature Condition Of Fuel Cell (320 K)											
VSS-P&O	112.5A	39.37 V	4429.5 W	8.1159A	526.40 V	4269.16 W	96.38%	0.028 s	No	High	Less
RBFN	113.2A	40.60 V	4600.2 W	8.460A	528.50 V	4471.2 W	97.19%	0.041 s	Yes	High	Less
FLC-VSSIC	113.7A	42.02 V	4780.1 W	8.751A	531.522 V	4650.82 W	97.29%	0.031 s	No	Medium	Moderate
FLC-IHC	112.8A	42.60 V	4805.3 W	8.8388A	533.61 V	4716.49 W	98.15%	0.15 s	No	Medium	Moderate
IBeta-FLC	109.5A	43.91 V	4809.7 W	8.8160A	538.88 V	4750.77 W	98.78%	0.18 s	No	Less	Less
Operating Temperature Condition Of Fuel Cell (300 K)											
VSS-P&O	105.1A	37.89 V	3979.0 W	7.675A	497.10 V	3815.51 W	95.89%	0.03 s	No	High	Less
RBFN	107.1A	38.60 V	4130.6 W	8.009A	499.22 V	3998.48 W	96.80%	0.04 s	Yes	High	Less
FLC-VSSIC	107.1A	40.02 V	4290.4 W	8.281A	501.60 V	4154.02 W	96.82%	0.033 s	No	Medium	Moderate
FLC-IHC	106.5A	40.33 V	4297.2 W	8.3161A	506.44 V	4211.31 W	98.00%	0.17 s	No	Medium	Moderate
IBeta-FLC	104.4A	41.05 V	4288.2 W	8.272A	510.27 V	4220.11 W	98.41%	0.22 s	No	Less	Less
Operating Temperature Condition Of Fuel Cell (340 K)											
VSS-P&O	118.2A	41.71 V	4932.1 W	8.577A	555.3 V	4763.15 W	96.57%	0.018 s	No	High	Less
RBFN	119.9A	42.68 V	5120.6 W	8.9462A	557.5 V	4987.55 W	97.39%	0.029 s	Yes	High	Less
FLC-VSSIC	120.0A	44.35 V	5318.6 W	9.246A	560.5 V	5182.5 W	97.44%	0.022 s	No	Medium	Moderate
FLC-IHC	120.2A	44.52 V	5352.4 W	9.294A	565.32 V	5256.04 W	98.20%	0.139 s	No	Medium	Moderate
IBeta-FLC	120.1A	44.55 V	5354.1 W	9.329A	566.09 V	5280.22 W	98.85%	0.155 s	No	Less	Less

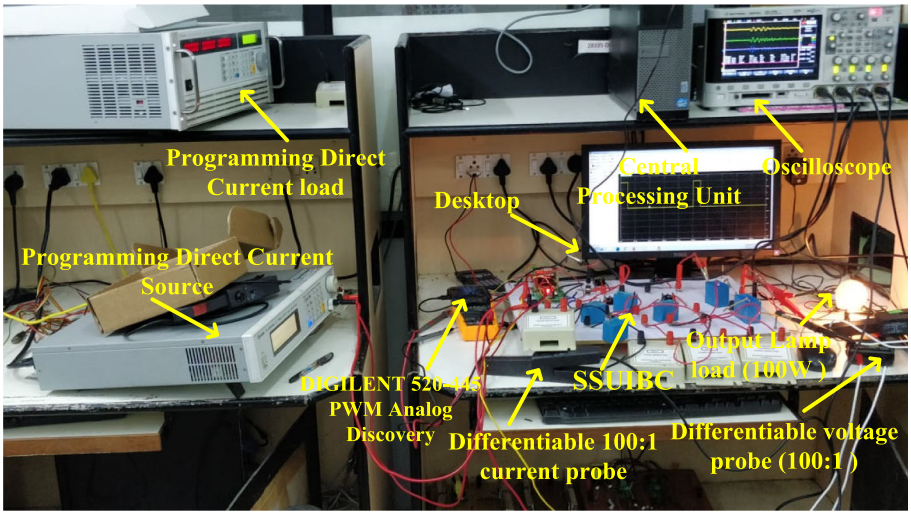

Fig. 16 Experimental setup for the non-isolated DC-DC converter

Table 6 Experimental design parameters of SSUIBC

Parameters	Values
Input voltage supply (V_i)	70.0 V
100:1 Voltage probes	0 to 5 kV
Gate driver circuit (TLP-250)	0 to 8.7 V
Lamp load	100 W
Converter operating frequency (f_s)	20 kHz
Type of MOSFET	IRF-640 N
Output voltage of converter (V_0)	122.9 V
Input side capacitor current (C_x)	594μA
Capacitor values (C_x, C_y, C_z, and C_a)	20.0μF
Output capacitor value (C_0)	50.0μF
Designed inductor values ((L_x, L_y, and L_z)	35.0μH
Diode voltages (D_x, D_y)	39.5 V, 36.18 V
Type of DSO	TPS-2024B

and 4750.77 W, respectively. From Fig. 14f, it is clearly observed that the efficiency of IBeta-FLC is 98.78% which is greater than the RBFN and VSS-P&O. In addition, the IBeta-FLC MPPT controller gives less steady-state oscillations across MPP, high tracking speed, and less design complexity when compared to the other MPPT controllers.

(b). Dynamic operating temperature condition of PEMFC (320 K, 300 K, and 340 K).

At the dynamic operating temperature condition of PEMFC, the IBeta-FLC is compared with other power point tracking controller in terms of settling time, tracking speed, fuel cell output power, and efficiency. From Fig. 15a, the fuel cell temperature starts increasing from 0 to 320 K (0 to 0.3 s). At 0.3 s, the temperature is suddenly stepped down to 300 K up to the period of 0.6 s. Finally, at 0.6 s, the fuel cell temperature is stepped up to 340 K. The performance of PEMFC fed SSUIBC system is analyzed at step varying temperature condition by using different hybrid and conventional MPPT techniques.

From Fig. 15b, c, and d, at 300 K, the extracted fuel output current, voltage, and power by applying FLC-VSSIC, FLC-IHC, and IBeta-FLC-based MPPT techniques are 107.1A, 40.2 V, 4290.4 W, 106.5A, 40.33 V, 4297.2 W, 104.4A, 41.05 V, and 4288.2 W, respectively. At 340 K, the operating duty cycles of SSUIBC by applying VSS-P&O, RBFN, and FLC-VSSIC MPPT techniques are 0.781, 0.774, and 0.8, respectively. The IBeta-FLC is used to obtain the optimum duty cycle (see in Fig. 15e) which is given to the high step-up boost converter in order to improve the voltage profile of the PEMFC stack.

The converter output current, output voltage, and output powers of RBFN-based controller are 8.9462A (see in Fig. 15f), 557.5 V, and 4987.55 W, respectively. The converter output power rising and settling time of IBeta-FLC-based power point tracking controller are 0.01 s, and 0.155 s, respectively. Hence, from the above observation, it is determined that the IBeta-FLC-based MPPT technique is giving good dynamic response and high tracking speed when compared to the other power point tracking controllers. The detailed analysis of proposed fuel cell fed SSUIBC by applying diverse MPP tracking controller is given in Table 5.

8 Experimental design and analysis of SSUIBC

Here, M62020P8058 programmed direct power supply is used to investigate and analyze the proposed single switch boost converter for fuel cell-based electric vehicle application as shown in Fig. 16. The high switching frequency-based Metal Oxide Field Effect Transistor switch is used in the proposed boost converter in order to reduce the overall

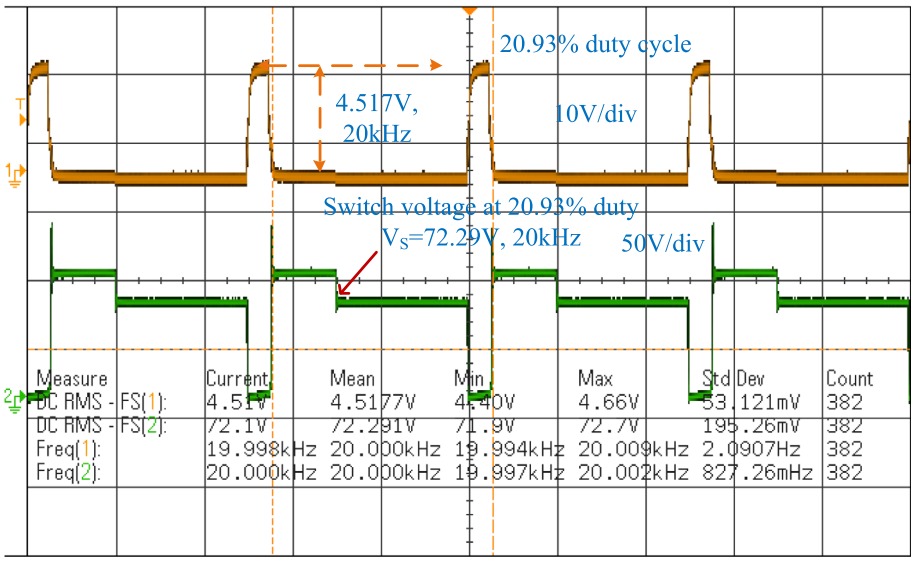

Fig. 17 MOSFET Switching pulses and its output voltage

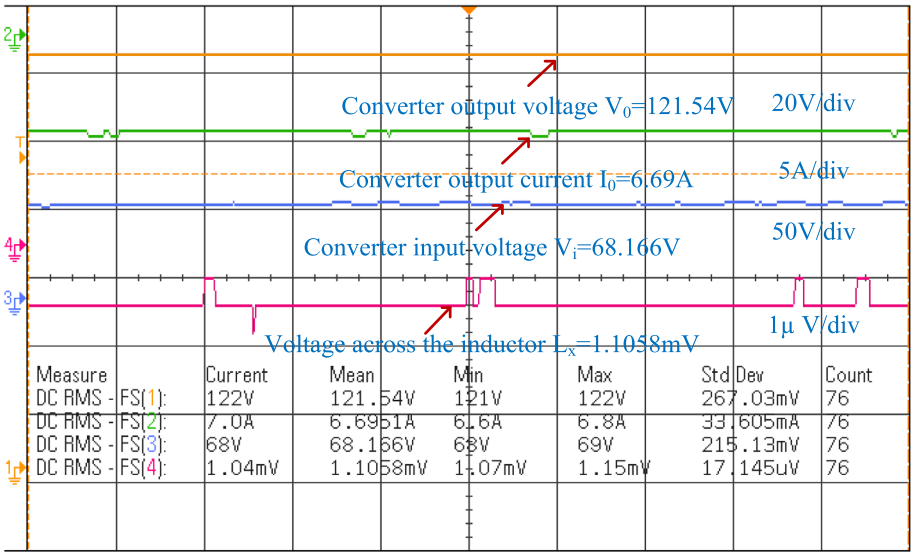

Fig. 18 SSUIBC output voltage, output current, input voltage and inductor voltage

system heat and conduction losses. In addition, its consumption and dissipation power losses are very less when compare to the BJT and IGBT. The experimental design parameters of SSUIBC are given in Table 6.

The analog discovery (Digilent 520-445) acts as a pulse width modulator in order to supply the switching pulses to the SSUIBC. The TLP-250 isolated MOSFET gate driver circuit is used to protect the power semiconductor devices from the sudden change of input voltages. The gate driver circuit consists of light-emitting diode (GaAlAs) which receives the signal from the source and it gives the signal to the PWM generator by using an integrated photo detector. The maximum operated voltage rating of the driver circuit is 4.66 V. The 4N28 optocoupler is connected between the control circuit and load to control the converter output voltage. The MOSFET operated frequency is 20 kHz, and the selected duty for analyzing the performance of SSUIBC is 20.93% (see in Fig. 17).

The optimum duty cycle is given to the single switch high step-up converter in order to boost the voltage from 68.166 to 121.54 V as shown in Fig. 18. From Fig. 18, it is observed that the current is stepped down and the voltage is stepped up. As a result, the converter reduces the overall system conduction losses and improves the efficiency.

9 Conclusion

The proposed IBeta-FLC-based MPPT technique performance is evaluated successfully in terms of converter output power, operating efficiency, settling time, design complexity, dependency on PV array, and oscillations

across MPP. The proposed MPPT technique is compared with other hybrid MPPT techniques. From the comparative simulation results, it is concluded that the proposed improved Beta-based fuzzy logic MPPT controller gives high MPP tracking speed and less oscillations. In addition, it gives optimum duty cycle to the fuel cell fed single switch boost converter. As a result, the overall system switching and conduction losses are reduced. Also, the proposed DC-DC converter is giving constant and continuous output voltage with less distortions. The features of SSUIBC are high voltage conversion ratio, wide input operation and less voltage stress on power semiconductor devices.

Funding The article is not receiving any funding.

Data availability The authors confirm that the data supporting the findings of this work are available within the article.

References

Ahmad S (2020) Design and analysis of a single switch DC–DC boost converter based on voltage lift technique. Diss. Department of Electrical and Electronic Engineering

Alajmi BN et al (2010) Fuzzy-logic-control approach of a modified hill-climbing method for maximum power point in microgrid standalone photovoltaic system. IEEE Trans Power Electron 26(4):1022–1030

Alaswad A et al (2021) Technical and commercial challenges of proton-exchange membrane (PEM) fuel cells. Energies 14(1):144

Aly M, Rezk H (2020) A differential evolution-based optimized fuzzy logic MPPT method for enhancing the maximum power extraction of proton exchange membrane fuel cells. IEEE Access 8:172219–172232

Banham D et al (2018) Critical advancements in achieving high power and stable nonprecious metal catalyst–based MEAs for real-world proton exchange membrane fuel cell applications. Sci Adv 4(3):1eaa117180

Fu Z et al (2021) Research on energy management strategy of fuel cell power generation system based on Grey–Markov chain power prediction. Energy Rep 7:319–325

Garrigós A et al (2019) Interleaved, switched-inductor, multi-phase, multi-device DC/DC boost converter for non-isolated and high conversion ratio fuel cell applications. Int J Hydrogen Energy 44(25):12783–12792

Habib M, Khoucha F, Harrag A (2017) GA-based robust LQR controller for interleaved boost DC–DC converter improving fuel cell voltage regulation. Electric Power Syst Res 152:438–456

Harrag A, Messalti S (2017) Variable step size IC MPPT controller for PEMFC power system improving static and dynamic performances. Fuel Cells 17(6):816–824

Harrag A, Messalti S (2018) How fuzzy logic can improve PEM fuel cell MPPT performances? Int J Hydrogen Energy 43(1):537–550

Harrag A, Rezk H (2021) Indirect P&O type-2 fuzzy-based adaptive step MPPT for proton exchange membrane fuel cell. Neural Comput Appl 1–14

Hasanpour S et al (2020) New semiquadratic high step-up DC/DC converter for renewable energy applications. IEEE Trans Power Electron 36(1):433–446

Ijaodola OS et al (2019) Energy efficiency improvements by investigating the water flooding management on proton exchange membrane fuel cell (PEMFC). Energy 179:246–267

Kaur R et al (2017) A novel proton exchange membrane fuel cell based power conversion system for telecom supply with genetic algorithm assisted intelligent interfacing converter. Energy Conver Manage 136:173–183

Kurnia JC et al (2021) Progress on open cathode proton exchange membrane fuel cell: Performance, designs, challenges and future directions. Appl Energy 283:116359

Li X et al (2020b) A novel assorted nonlinear stabilizer for DC–DC multilevel boost converter with constant power load in DC microgrid. IEEE Trans Power Electron

Li G et al (2020a) A novel quadratic boost converter with low inductor currents. CPSS Trans Power Electron Appl 5(1):1–10

Lin-Kwong-Chon C et al (2019) A review of adaptive neural control applied to proton exchange membrane fuel cell systems. Ann Rev Control 47:133–154

Ma R et al (2019) Advanced robustness control of DC–DC converter for proton exchange membrane fuel cell applications. IEEE Trans Ind Appl 55(6):6389–6400

Mallick N, Mukherjee V (2020) Maximum power point tracking supported proton exchange membrane fuel cell based intelligent dynamic voltage restorer. Int J Hydrogen Energy 45(53):29271–29287

Naseri N et al (2018) Proton exchange membrane fuel cell modelling and power control by P&O algorithm. In: 2018 6th International Renewable and Sustainable Energy Conference (IRSEC). IEEE

Sadaghati F et al (2020) A high step-up transformer-less DC–DC converter with continuous input current. In: 2020 11th power electronics, drive systems, and technologies conference (PEDSTC). IEEE

Salvado MB et al (2021) Towards the understanding of transport limitations in a proton-exchange membrane fuel cell catalyst layer: performing agglomerate scale direct numerical simulations on electron-microscopy-based geometries. J Power Sources 482:228893

Shetty N, Chakrasali RL (2020) Power management in a hybrid grid involving photo voltaic and proton exchange membrane fuel cell. Sensor Lett 18(4):259–267

Srinivasan S et al (2021) Neural network based MPPT control with reconfigured quadratic boost converter for fuel cell application. Int J Hydrogen Energy 46(9):6709–6719

Thounthong P et al (2021) Design and control of multiphase interleaved boost converters-based on differential flatness theory for PEM fuel cell multi-stack applications. Int J Electr Power Energy Syst 124:106346

Török L et al (2019) Optimization of isolated DC-DC converter topologies for fuel cell applications. In: 2019 21st European Conference on Power Electronics and Applications (EPE'19 ECCE Europe). IEEE

Uthirasamy R et al (2020) Extended Boost DC-DC-AC converter for electric vehicle applications. In: IOP conference series: materials science and engineering, vol. 937. No. 1. IOP Publishing

Villarreal-Hernandez CA et al (2020) A double dual boost converter with switching ripple cancellation for PEMFC systems. Electronics 9(10):1592

Youn H-S et al (2020) Study on boost converters with high power-density for hydrogen-fuel-cell hybrid railway system. Electronics 9(5):771

Zakaria Z et al (2021) The progress of fuel cell for malaysian residential consumption: Energy status and prospects to

introduction as a renewable power generation system. Renew Sustain Energy Rev 144:110984
Zhang Li, Wang N (2018) Application of coRNA-GA based RBF-NN to model proton exchange membrane fuel cells. Int J Hydrogen Energy 43(1):329–340
Zhou M et al (2019) Research on composite control strategy of quasi-Z-source DC–DC converter for fuel cell vehicles. Appl Sci 9(16):3309